IEEE Access
Multidisciplinary ⋮ Rapid Review ⋮ Open Access Journal

Received 8 September 2024, accepted 22 September 2024, date of publication 25 September 2024,
date of current version 11 October 2024.

Digital Object Identifier 10.1109/ACCESS.2024.3467950

RESEARCH ARTICLE

Frequency Division Cooperation-Based Folding Steering Control for Distributed-Drive Articulated Steering Vehicles

ZHIYONG JI[1], ZHONGBIN WU[1,2], HAOWEN LI[1], YANSONG ZHAO[1], AND TIE WANG[1,3]
[1]College of Mechanical and Vehicle Engineering, Taiyuan University of Technology, Taiyuan 030024, China
[2]Taiyuan Research Institute Company Ltd., China Coal Technology and Engineering Group, Taiyuan 030024, China
[3]Centre for Efficiency and Performance Engineering, University of Huddersfield, Queensgate, HD1 3DH Huddersfield, U.K.

Corresponding authors: Zhongbin Wu (wuzhongbin01@tyut.edu.cn) and Tie Wang (wangtie57@163.com)

This work was supported in part by the National Natural Science Foundation of China under Grant 52204173, and in part by Shanxi Provincial Basic Research Program Youth Science Research Fund under Grant 20210302124118.

ABSTRACT The traditional articulated steering vehicles rely on the hydraulic steering system and segmented body structure to achieve vehicle steering. The folding steering process exhibits strong hysteresis, which reduces the steering maneuverability and also impacts the autonomous driving performance. This paper proposes a novel control method of folding steering based on differential-hydraulic frequency division cooperation for the redundant drive characteristic of distributed-drive articulated steering vehicles. The main contributions of this paper are as follows: 1) By introducing the speed term into the folding angle control, a position-velocity double closed-loop structure is employed to determine the steering demand torque and achieve the variable steering ratio and accurate control of the folding angle. 2) According to the frequency-domain characteristics of the hydraulic and differential steering systems, a first-order low-pass filtering algorithm is utilized to decompose the steering demand torque into high-frequency and low-frequency components. The high-frequency torque is borne by the differential system, while the low-frequency torque is borne by the hydraulic system, thereby addressing the challenge of cooperative control of multiple actuators. 3) An experimental platform for the distributed-drive articulated steering vehicle is constructed, and the credibility of the dynamic model is experimentally validated. 4) The manipulation and path-tracking performances of the proposed folding steering control method are analyzed. The results indicate that, compared to the hydraulic steering system, the average folding angle rise time and phase delay are reduced by 19.8% and 44.4%, respectively, significantly improving the follow-up performance of folding steering. Furthermore, the average lateral position error and heading angle error in path tracking control are reduced by 38.1% and 27.5%, respectively, which contribute to the electrification and intelligent development of articulated steering vehicles.

INDEX TERMS Articulated steering vehicles, distributed driving, differential-hydraulic frequency division cooperation, folding steering control, path tracking.

I. INTRODUCTION

Articulated steering vehicles (ASVs) are a kind of low-speed, special-operation vehicle suitable for driving on all-terrain surfaces and in narrow spaces. They consist of two vehicle bodies and are connected by an intermediate articulated mechanism, which has the advantages of a small steering radius, large load capacity, and high flexibility. ASVs are widely used in the fields of mining, construction, and agriculture. References [1] and [2], especially in the mining trackless auxiliary transport and operation system, where they play an important role and effectively reduce manual labor intensity and safety risks [3].

The associate editor coordinating the review of this manuscript and approving it for publication was Azwirman Gusrialdi.

The traditional ASVs adopt the centralized drive and hydraulic steering, resulting in low control freedom for the whole vehicle [4], [5]. With the advancement of electronic control technology, the ASVs are gradually developing towards distributed electric drive and composite steering, i.e., distributed-drive articulated steering vehicles (DASV), significantly enhancing vehicle control flexibility [6]. In recent years, numerous scholars have conducted extensive research on the performance optimization of the hydraulic system, energy consumption control, and path tracking control of DASVs, achieving notable results [7], [8], [9], [10], [11], [12]. In [7], a differential drive collaborative steering (DDCS) method is proposed, which utilizes differential torque to overcome steering resistance, thereby reducing energy consumption of the steering system. The influence of DDCS on vehicle motion and the differential torque axis distribution coefficient on drive system energy consumption is explored. In [9], the stability difference between the nonlinear and linear models of ASVs under the action of external disturbances is analyzed, and a new method to improve the stability of ASVs by controlling the oil filling pressure is proposed, which has the advantages of simple control and lower energy consumption. In [12], a path-tracking control method is proposed that combines preview control with sideslip compensation. This compensation mechanism is used to further eliminate tracking errors under sideslip conditions, thereby not only improving control accuracy but also accelerating convergence speed. However, the unique characteristics of ASVs, such as body structure, steering mode, and driving conditions, lead to strong nonlinear and hysteresis of the folding steering system [6], [13], which restricts the improvement of vehicle maneuverability and driving safety, as well as the application of autonomous driving technology. Therefore, it is necessary to conduct more intensive research on the folding steering performance of DASVs.

At present, the folding steering methods of DASVs are divided into three types: hydraulic steering, differential steering, and differential-hydraulic cooperative steering. The hydraulic steering method achieves folding steering by pushing the relative rotation of the front and rear bodies around the articulation point, utilizing the expansion and contraction movements of hydraulic cylinders arranged symmetrically on both sides of the vehicle body. Due to the hydraulic system suffers from numerous transmission links, poor sealing of components, the compressibility of the oil, and other problems, resulting in poor response speed and energy utilization [14]. Additionally, the range of the folding angle will be limited by the stroke of the hydraulic cylinder [15]. However, its high power density can provide sufficient steering torque, and the hydraulic system has a certain damping, which contributes to the steering stability of the vehicle [16]. The differential steering method does not require special steering devices. By controlling the output torque of the driving motors on the left and right sides of the vehicle, the longitudinal forces acting on the inside and outside wheels are altered, thereby generating a yaw moment that drives the vehicle to change its folding angle [17]. Based on the advantage of the DASVs can independently control the driving force of each wheel, the differential steering method offers faster response speed and higher energy utilization [18], [19]. In [1] and [6], both studies use the yaw velocity of the vehicle body as a reference and design a direct yaw moment control system using a sliding mode controller (SMC) and a combined algorithm of composite nonlinear feedback and active disturbance rejection control (CNF+ADRC), respectively. In this manner, the differential steering method completely replaces the hydraulic steering method, improving the steering response performance and path-tracking control accuracy of the vehicle. However, the magnitude of the differential steering torque is limited by the performance of the drive motors and the adhesion condition of the wheels. Additionally, because there is no additional support at the articulation point, the vehicle body is more prone to swaying behavior under the action of external interference.

The differential-hydraulic cooperative steering method effectively combines the advantages of both steering methods. The differential torque generated by each wheel can assist the hydraulic steering system to operate more efficiently and improve the response performance of the vehicle steering [17]. Simultaneously, the intervention of differential steering will inevitably share part of the steering resistance, thereby reducing the working pressure and energy consumption of the hydraulic system. Furthermore, the stability of folding steering can be improved by absorbing the fluctuations of the steering demand torque through the appropriate yaw moment [20], [21]. To obtain the appropriate yaw moment, in [22], a direct yaw torque control strategy is designed based on feedforward and feedback compensation by using a 3-DOF model as the steering reference model, with the yaw velocity and the sideslip angle of the center of mass of the front and the rear bodies as the control variables. In [23], the feedforward and feedback control strategy is also adopted, but it adds the Ackermann steering geometry relationship in the 2-DOF reference model to determine the feedforward control quantity of the direct yaw moment and utilizes the linear quadratic regulator (LQR) to calculate the feedback compensation control quantity. In [24], by linearizing and discretizing the vehicle mathematical model, the MPC method was used to calculate the direct yaw moment required by the front and rear bodies under external disturbances, aiming to reduce their impact on vehicle stability. Although the application of various intelligent algorithms enables precise calculation of the required yaw steering torque, the output of the hydraulic steering system is not fully considered, i.e., the coupling manner of the two steering modes, so it is difficult to form a favorable cooperation with the hydraulic steering system.

All the above researches focus on the energy saving and stability control problems in the steering process of ASVs, and the lack of research on the follow-up performance in

the folding process. Specifically, the whole vehicle steering process of ASVs can be divided into two stages: folding and steering. Among them, the folding stage refers to the process from the steering command to the change of the folding angle (the angle of relative rotation of the vehicle body on both sides of the articulation point), and its main index is the rapidity and accuracy, i.e., the folding angle needs to respond to the steering command quickly so that the vehicle can adjust the attitude in time. At the same time, the folding process needs to be precisely controlled to ensure the accuracy and safety of the steering. The steering stage refers to the process from the steering command to the change of the vehicle heading angle (the angle of the vehicle relative to the geodetic coordinate system), and its main index is stability to avoid the occurrence of dangerous situations such as yaw, overturning, and skidding. Since the heading change of ASVs is realized by the folding motion, the folding process is a prerequisite for the steering, which has a significant influence on the steering performance of the whole vehicle.

Different from the previous research, this paper focuses on the folding process of DASVs. The primary objective is to improve the follow-up performance of folding steering and address the coupling problem between differential and hydraulic steering. To achieve this, by fully utilizing the characteristics of the rapid motor response and redundant drive of the DASVs, and the precision control offered by the double closed-loop control structure, a folding steering control method based on differential-hydraulic frequency division coordination is proposed. The overall control idea is as follows: the vehicle steering demand torque is determined based on the deviations of the target steering angle and steering velocity from the actual feedback of the vehicle folding angle and folding velocity, and then the steering demand torque is divided into high-frequency torque and low-frequency torque by a low-pass filtering algorithm. The high-frequency torque is converted into the driving torque of each wheel through the differential torque distribution model. The low-frequency torque is converted into the input and output pressure of the hydraulic cylinder through the inverse dynamics model of the hydraulic steering system, and then the hydraulic steering control system controls the thrust generated by the hydraulic cylinder acting on the front and rear bodies. Considering that the filter coefficient significantly impacts the low-pass filtering outcome, the turning point of the phase delay trend for the hydraulic steering system is used as the cut-off frequency to determine the filter coefficient. This approach ensures a rational distribution of the steering demand torque. The final analysis is not only concerned with the performance index of the folding process itself but also investigates its influence on path tracking control.

The rest of the paper is organized as follows: In Section II, the nonlinear vehicle dynamics model of DASVs is established. In Section III, the folding steering control strategy based on differential-hydraulic frequency division cooperation is introduced in detail. In Section IV, the whole vehicle model is experimentally validated and the performance of the proposed method is analyzed in terms of folding follow-up performance and path tracking performance, respectively. Finally, the main conclusions are given in Section V.

II. DYNAMIC MODEL OF DASVs

A. VEHICLE BODY MODEL

Assuming that the vehicle travels on a flat road surface and neglecting the effects of slope gradients and air resistance, the DASVs can be described as a vehicle model with eight degrees of freedom, including longitudinal, lateral, and yaw movement of the front body, yaw movement of the rear body, and rotational motions of the four wheels. As shown in Fig. 1, $O_1X_1Y_1$ and $O_2X_2Y_2$ are the local coordinates of the center of mass for the front and rear bodies, respectively. The moment subjected to the vehicle body is positive in the clockwise direction and negative in the counterclockwise direction. The force direction is positive in the coordinate system direction and negative in the reverse direction.

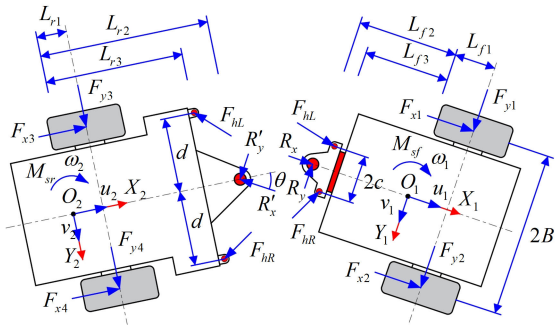

FIGURE 1. Force diagram of the DASVs.

According to the force balance at the articulation point and the vehicle kinematic relationship, the dynamic differential equations of the forces and moments of the front and rear bodies in the longitudinal, lateral, and yaw directions are established as follows:

$$\begin{cases} m_1\left(\dot{u}_1 - v_1\omega_1\right) = F_{txf} + F_{hxf} + R_x \\ m_1\left(\dot{v}_1 + u_1\omega_1\right) = F_{tyf} + F_{hyf} - R_y \\ I_1\dot{\omega}_1 = M_{txf} + M_{tyf} + M_{sf} + R_y L_{f2} \end{cases} \tag{1}$$

$$\begin{cases} m_2\left(\dot{u}_2 - v_2\omega_2\right) = F_{txr} - F_{hxr} - R_x\cos\theta - R_y\sin\theta \\ m_2\left(\dot{v}_2 + u_2\omega_2\right) = F_{tyr} + F_{hyr} - R_x\sin\theta + R_y\cos\theta \\ I_2\dot{\omega}_2 = M_{txr} + M_{tyr} + M_{sr} + (R_y\cos\theta - R_x\sin\theta)L_{r1} \end{cases} \tag{2}$$

where θ is the folding angle, u_1 and u_2 are the longitudinal speed of the front and rear bodies, v_1 and v_2 are the lateral speed of the front and rear bodies, m_1 and m_2 are the mass of the front and rear bodies, I_1 and I_2 are the moment of inertia of the front and rear bodies around the center of mass, ω_1 and ω_2 are the yaw velocity of the front and rear bodies around the center of mass, R_x, R_y, R'_x, and R'_y are the internal force of the interaction between the two bodies at the articulation

point, $R'_x = -R_x$, $R'_y = -R_y$. The remaining variables are defined as follows.

The equivalent resultant forces along the X-axis and Y-axis of the center of mass, and the moment around the Z-axis, which are generated by the longitudinal and lateral forces acting on the wheels, are expressed as:

$$\begin{cases} F_{txf} = F_{x1} + F_{x2} \\ F_{tyf} = F_{y1} + F_{y2} \\ F_{txr} = F_{x3} + F_{x4} \\ F_{tyr} = F_{y3} + F_{y4} \end{cases} \tag{3}$$

$$\begin{cases} M_{txf} = (F_{x1} - F_{x2})B \\ M_{tyf} = (F_{y1} + F_{y2})L_{f1} \\ M_{txr} = (F_{x3} - F_{x4})B \\ M_{tyr} = (F_{y3} + F_{y4})L_{r1} \end{cases} \tag{4}$$

where F_{xi} and F_{yi} are the longitudinal and lateral forces of each wheel, $i \in (1-4)$ representing the left front, right front, left rear, and right rear wheels, respectively, B is half of the wheelbase, L_{f1} and L_{r1} are the distance from the center of mass of the front and rear bodies to the axles of their respective body, respectively.

The equivalent component forces of the hydraulic cylinder thrust along the X-axis and Y-axis of the front and rear bodies are expressed as:

$$\begin{cases} F_{hxf} = F_{hL}\cos\alpha_1 + F_{hR}\cos\alpha_2 \\ F_{hyf} = F_{hL}\sin\alpha_1 - F_{hR}\sin\alpha_2 \\ F_{hxr} = F_{hL}\cos\alpha_3 + F_{hR}\cos\alpha_4 \\ F_{hyr} = F_{hR}\sin\alpha_4 - F_{hL}\sin\alpha_3 \end{cases} \tag{5}$$

where F_{hL} and F_{hR} are the thrust force of the left and right hydraulic cylinders, and α_i, $i \in (1-4)$ is the angle between the axis of the hydraulic cylinder and the longitudinal axis of the front body and rear body, respectively, as shown in Fig. 2.

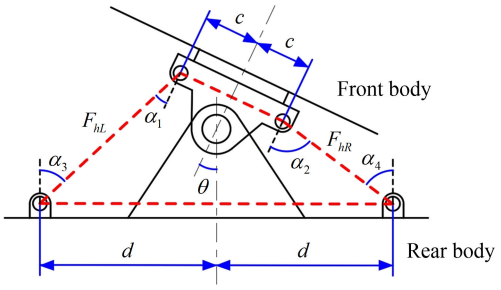

FIGURE 2. Schematic diagram of articulated steering structure.

The yaw moments generated by the hydraulic cylinder thrust around the Z-axis at the center of mass of the front and rear bodies are expressed as:

$$\begin{cases} M_{sf} = \Delta F_{hxf}\, c + \Delta F_{hyf} L_{f3} \\ M_{sr} = \Delta F_{hxr} d + \Delta F_{hyr} L_{r3} \end{cases} \tag{6}$$

$$\begin{cases} \Delta F_{hxf} = F_{hL}\cos\alpha_1 - F_{hR}\cos\alpha_2 \\ \Delta F_{hyf} = -F_{hL}\sin\alpha_1 + F_{hR}\sin\alpha_2 \\ \Delta F_{hxr} = -F_{hL}\cos\alpha_3 + F_{hR}\cos\alpha_4 \\ \Delta F_{hyr} = -F_{hL}\sin\alpha_3 + F_{hR}\sin\alpha_4 \end{cases} \tag{7}$$

Since the front and rear bodies are connected via the steering pin, their velocities at the steering pin are equal. Consequently, the motion state of the rear body relative to the front body can be described as:

$$\begin{cases} \theta = \int_0^t (\omega_1 - \omega_2)dt \\ u_2 = u_1\cos\theta - (v_1 - L_{f2}\omega_1)\sin\theta \\ v_2 + L_{r1}\omega_2 = u_1\sin\theta + (v_1 - L_{f2}\omega_1)\cos\theta \end{cases} \tag{8}$$

The angular speed of wheel rotation ω_{ti} is related to the motor driving torque T_{mi}, then the differential equation of wheel rotation dynamics can be expressed as:

$$I_t\dot{\omega}_{ti} = T_{mi}i_0\eta - (f_sF_{zi} + F_{xi})r_w \tag{9}$$

where I_t is the moment of inertia of the wheel, i_0 is the transmission ratio of the wheel reducer, η is the transmission efficiency, f_s is the rolling resistance coefficient of the wheel, r_w is the rolling radius of the wheel, F_{zi} is the vertical load of the tire, $i \in (1-4)$.

According to the kinematic constraints between the front and rear bodies, and eliminating the internal forces R_x and R_y at the articulation point, the vehicle dynamics model is shown in (10). Among them, the inputs of the vehicle dynamics model are the hydraulic cylinder thrust F_{hL} and F_{hR}, and the tire force F_{tx} and F_{ty}. The outputs are the velocity u_1 and v_1 of the front body, the yaw velocity ω_1 and ω_2, and the rotational velocity ω_{ti} of the wheel. Other vehicle parameters, such as folding angle θ, rear body speed u_2 and v_2, can be further derived from the above outputs.

$$\begin{cases} (m_1+m_2)\dot{u}_1 - m_2L_{r2}\dot{\omega}_2\sin\theta = (m_1+m_2)v_1\omega_1 \cdots \\ -m_2L_{f2}\omega_1^2 - m_2L_{r2}\omega_2^2\cos\theta + F_{txr}\cos\theta + F_{txf} \cdots \\ +F_{tyr}\sin\theta + F_{hxr}\cos\theta + F_{hyr}\sin\theta + F_{hxf} \\ (m_1+m_2)\dot{v}_1 - m_2L_{f2}\dot{\omega}_1 - m_2L_{r2}\dot{\omega}_2\cos\theta = F_{tyf} \cdots \\ -(m_1+m_2)u_1\omega_1 + m_2L_{r2}\omega_2^2\sin\theta + F_{tyr}\cos\theta \cdots \\ -F_{txr}\sin\theta - F_{hxr}\sin\theta + F_{hyr}\cos\theta + F_{hyf} \\ m_1L_{f2}\dot{v}_1 + I_1\dot{\omega}_1 = -m_1L_{f2}u_1\omega_1 + F_{tyf}L_{f2} + M_{txf} \cdots \\ +F_{hyf}L_{f2} + M_{tyf} + M_{sf} \\ m_1L_{r2}\dot{u}_1\sin\theta + m_1L_{r2}\dot{v}_1\cos\theta + I_2\dot{\omega}_2 = M_{txr} \cdots \\ -m_1u_1L_{r2}\omega_1\cos\theta + F_{tyf}L_{r2}\cos\theta + M_{tyr} \cdots \\ +m_1v_1L_{r2}\omega_1\sin\theta + F_{hxf}L_{r2}\sin\theta + M_{sr} \cdots \\ +F_{txf}L_{r2}\sin\theta + F_{hyf}L_{r2}\cos\theta \\ I_t\dot{\omega}_{ti} = T_{mi}i_0\eta - (f_sF_{zi} + F_{xi})r \end{cases} \tag{10}$$

B. TIRE MODEL

As an important medium for the interaction between the vehicle and the ground, the tire provides various input

forces needed in the vehicle [25]. The Fiala tire model is a dimensionless analytic formula derived from the simplified theoretical model of the tire, which can calculate the change law of longitudinal force and lateral force with the slip rate and sideslip angle [26]. Compared with other tire models, the Fiala tire model has the advantages of simple form, small calculation amount, and strong versatility, and it has high accuracy under good steering conditions excluding longitudinal and lateral combined slip [27]. The longitudinal force F_x is:

$$F_x = \begin{cases} K_x s, & |s| \le S_{sc} \\ sign(s)\left(\mu |F_z| - \left|\dfrac{(\mu F_z)^2}{4sK_x}\right|\right), & |s| > S_{sc} \end{cases} \tag{11}$$

$$S_{sc} = \left|\frac{\mu F_z}{2K_x}\right| \tag{12}$$

where K_x is the tire longitudinal stiffness, S_{sc} is the critical point of rolling and sliding at the tire grounding mark. When $|s| \le S_{sc}$, the tire is rolling. When $|s| > S_{sc}$, the tire is sliding. μ is the friction coefficient between the tire and the road surface, which is a function of the static friction coefficient μ_s when the wheel is pure rolling ($s = 0$), the kinetic friction coefficient μ_k when the wheel is pure sliding ($s = 1$), and the tire slip rate s, expressed as:

$$\mu = \mu_s - (\mu_s - \mu_k)\sqrt{s^2 + \tan^2(\alpha)} \tag{13}$$

The lateral force F_y is:

$$F_y = \begin{cases} -\mu |F_z| (1 - H^3) sign(\alpha_t) + \gamma K_\gamma, & |\alpha_t| \le \alpha_c \\ -\mu |F_z| \, sign(\alpha_t), & |\alpha_t| > \alpha_c \end{cases} \tag{14}$$

$$H = 1 - \frac{K_y |\tan(\alpha)|}{3\mu |F_z|} \tag{15}$$

$$\alpha_c = \arctan\left(\frac{3\mu |F_z|}{K_y}\right) \tag{16}$$

where K_y is the tire lateral stiffness, K_γ is the tire camber stiffness, γ is the tire camber angle, α_t is the tire sideslip angle, α_c is the critical point of rolling and sliding at the tire grounding mark, when $|\alpha_t| \le \alpha_c$, the tire is rolling, when $|\alpha_t| > \alpha_c$, the tire is sliding.

C. HYDRAULIC STEERING SYSTEM MODEL

The hydraulic steering system adopts the structure form of a symmetrical valve controlling an asymmetric hydraulic cylinder, and the main components include a three-position four-way electro-hydraulic proportional directional valve, hydraulic cylinder, and hydraulic pump station, as shown in Fig. 3.

The displacement of the valve spool and differential pressure determine the flow rate at the inlet and outlet of the electro-hydraulic proportional directional valve. Therefore, the load flow equation for the oil inlet and oil return circuit in

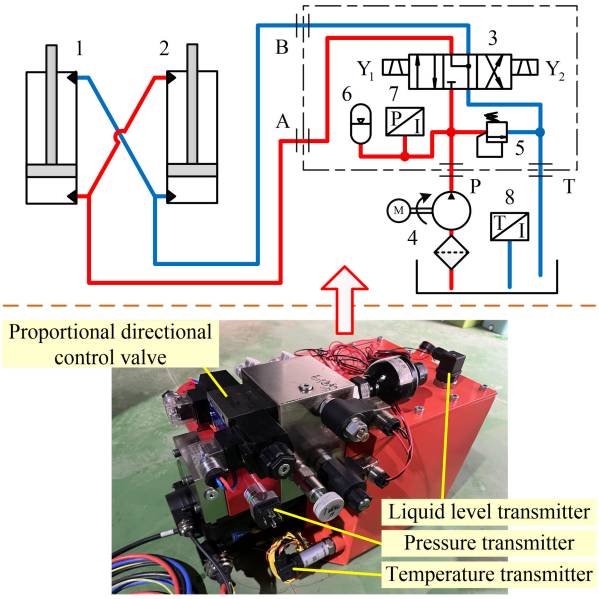

FIGURE 3. The overall structure of the hydraulic steering system: 1-left side hydraulic cylinder, 2-right side hydraulic cylinder, 3-proportional direction valve, 4-oil pump, 5-overflow valve, 6-hydraulic accumulator, 7-pressure transmitter, 8-temperature transmitter.

the hydraulic steering system is as follows:

$$\begin{cases} q_1 = C_d w x_e \sqrt{2(p_s - p_1)/\rho} \\ q_2 = C_d w x_e \sqrt{2(p_2 - p_0)/\rho} \end{cases} \tag{17}$$

where q_1 and q_2 are the flow rate at the inlet and outlet of the valve, C_d is the flow coefficient, w is the area gradient of valve port, and $w = A_{\max}/x_{\max}$, p_s and p_0 is the oil supply pressure and return pressure for the hydraulic system, $p_1$and p_2 is the oil inlet pressure and return pressure of the hydraulic cylinder, ρ is the density of hydraulic oil, x_e is the displacement of value spool, and $x_e = K_i i_c$, i_c is the control current of the proportional electromagnet, the positive current indicates that the hydraulic oil flows from port P to port A, and the negative current indicates that the hydraulic oil flows from port P to port B.

The flow rate at the inlet and outlet of the steering system consists of two parts, expressed as:

$$\begin{cases} q_1 = q_{L1} + q_{R2}, q_2 = q_{L2} + q_{R1} & i_c > 0.25 \\ q_1 = 0, q_2 = 0 & -0.25 \le i_c \le 0.25 \\ q_1 = q_{L2} + q_{R1}, q_2 = q_{L1} + q_{R2} & i_c < -0.25 \end{cases} \tag{18}$$

where q_{L1}, q_{L2}, q_{R1}, and q_{R2} are the flow rates of the rodless and rodded chamber of the left and right hydraulic cylinders, respectively, expressed as (19) and (20), shown at the bottom of the next page, where A_1 and A_2 are the areas of the rodless and rodded chamber of the hydraulic cylinder, respectively, E_1 is the elastic modulus of oil, $C_i$and C_e are the internal and external leakage coefficients of the hydraulic cylinder, V_{ij} and $p_{ij} (i = L, R, \quad j = 1, 2)$ are the oil volume and pressure for the rodless and rodded chamber of the left and right hydraulic cylinder, respectively, $\Delta p_L = p_{L1} - p_{L2}$,

$\Delta p_R = p_{R1} - p_{R2}$, ΔX_L and ΔX_R are the changes in the length of the left and right hydraulic cylinder, respectively, where a positive value indicates that the hydraulic cylinder is extended, and a negative value indicates that it is shortened, and $\Delta X_L = X_L - X_{L0}$, $\Delta X_R = X_R - X_{R0}$, X_L and X_R are the length of the left and right hydraulic cylinder when steering, X_{L0} and X_{R0} are the initial length of the left and right hydraulic cylinders, respectively.

According to the directional characteristics of the hydraulic cylinder and the proportional valve, it is known that:

$$\begin{cases} p_1 = p_{L1} = p_{R2},\ p_2 = p_{R1} = p_{L2} & i_c > 0.25 \\ p_1 = p_{R1} = p_{L2},\ p_2 = p_{R2} = p_{L1} & i_c < -0.25 \end{cases} \tag{21}$$

The oil volume of each chamber of the hydraulic cylinder is expressed as:

$$\begin{cases} V_{L1} = A_1(l_1 + \Delta X_{\mathrm{L}}) \\ V_{L2} = A_2(l_2 - \Delta X_L) \\ V_{R1} = A_1(l_1 + \Delta X_R) \\ V_{R2} = A_2(l_2 - \Delta X_R) \end{cases} \tag{22}$$

where l_1 and l_2 is the length of the rodless and rodded chambers of the hydraulic cylinder at the beginning.

Based on (18) and combined with (19) to (22), the differential equation of oil pressure p_1 and p_2 can be obtained as follows (23)–(25), shown at the bottom of the next page.
where V_1 and V_2 are the oil volume of the hydraulic cylinder, and $V_1 = V_{L1} + V_{R2}$, $V_2 = V_{R1} + V_{L2}$.

Then the left and right hydraulic cylinder thrust F_{hL} and F_{hR} are expressed as:

$$\begin{cases} F_{hL} = A_1 p_{L1} - A_2 p_{L2} - f_{s1}\Delta\dot{X}_L \\ F_{hR} = A_1 p_{R1} - A_2 p_{R2} - f_{s1}\Delta\dot{X}_R \end{cases} \tag{26}$$

where f_{s1} is the coefficient of kinetic friction.

By bringing the hydraulic cylinder thrust F_{hL} and F_{hR}, wheel force F_x and F_y into the vehicle body model, the vehicle nonlinear dynamics model coupled with the steering system and tire model of DASVs can be obtained.

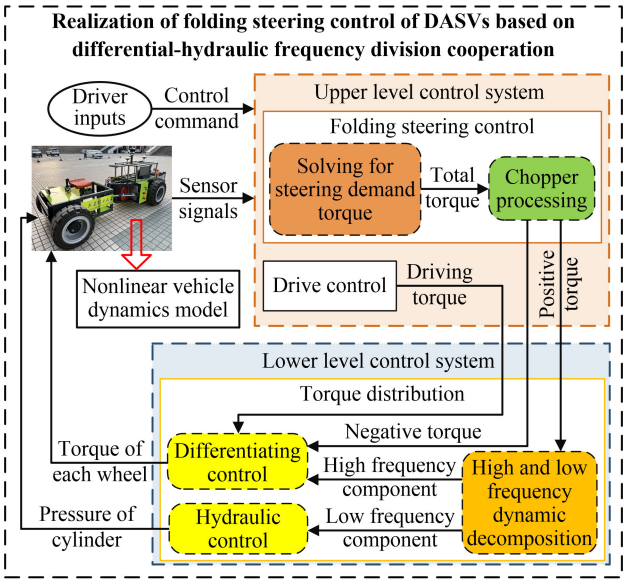

FIGURE 4. The workflow of the proposed steering control strategy.

III. FOLDING STEERING CONTROL EMPLOYING DIFFERENTIAL-HYDRAULIC FREQUENCY DIVISION COOPERATION

The control system employs a hierarchical architecture, with the upper level determining the folding steering torque and driving torque, and the lower level distributing the target torque to each actuator. The overall workflow of this control strategy is shown in Fig. 4. The upper level control system solves the steering demand torque based on the steering command and the vehicle state information. To avoid the hydraulic pressure shock generated in the switching process of positive and negative steering torque, the chopper regulator is used to divide the vehicle steering torque into positive torque (the torque in the same direction of the folding velocity) and negative torque (the torque in the opposite direction of the folding velocity). The lower level control system inputs the positive torque into the high and low-frequency dynamic distribution model and is further decomposed into low-frequency components and high-frequency components by frequency division processing. To ensure the basic steering ability, the low-frequency positive torque is executed by

$$\begin{cases} q_{L1} = A_1\Delta\dot{X}_L + \dot{p}_{L1}V_{L1}/E_1 + C_i\Delta p_L + C_e p_{L1} \\ q_{R2} = -A_2\Delta\dot{X}_R + \dot{p}_{R2}V_{R2}/E_1 - C_i\Delta p_R + C_e p_{R2} \\ q_{R1} = -A_1\Delta\dot{X}_R - \dot{p}_{R1}V_{R1}/E_1 - C_i\Delta p_R + C_e p_{R1} \\ q_{L2} = A_2\Delta\dot{X}_L - \dot{p}_{L2}V_{L2}/E_1 + C_i\Delta p_L + C_e p_{L2} \end{cases} \quad i_c > 0.25 \tag{19}$$

$$\begin{cases} q_{L1} = -A_1\Delta\dot{X}_L - \dot{p}_{L1}V_{L1}/E_1 - C_i\Delta p_L + C_e p_{L1} \\ q_{R2} = A_2\Delta\dot{X}_R - \dot{p}_{R2}V_{R2}/E_1 + C_i\Delta p_R + C_e p_{R2} \\ q_{R1} = A_1\Delta\dot{X}_R + \dot{p}_{R1}V_{R1}/E_1 + C_i\Delta p_R + C_e p_{R1} \\ q_{L2} = -A_2\Delta\dot{X}_L + \dot{p}_{L2}V_{L2}/E_1 - C_i\Delta p_L + C_e p_{L2} \end{cases} \quad i_c < -0.25 \tag{20}$$

the hydraulic steering mechanism. To improve the responsiveness of the vehicle folding steering, the high-frequency positive torque and all negative torque are executed by the differential steering mechanism, so that the hydraulic and differential steering form a favorable cooperation. Finally, the target pressure of the hydraulic cylinders and the target torque of each driving wheel are calculated by the hydraulic control model and the differential control model. The specific design process of the controller is as follows.

A. STEERING TORQUE SOLUTION BASED ON POSITION-SPEED DOUBLE-LOOP REGULATION

The ideal steering control necessitates simultaneous control over both speed and position. Therefore, the speed term is incorporated into the position control loop to improve the system response performance from an internal control perspective. The controller structure of double closed-loop control of both folding position and speed for ASVs is shown in Fig. 5. Among them, the input of the position loop is the target steering angle and the actual folding angle of the vehicle, and the output is the folding velocity. The role of the position loop is to enable the vehicle to follow the target steering angle issued by the driver. The input of the speed loop is the folding velocity output by the position loop and the actual folding velocity of the vehicle, and the output is the whole vehicle steering demand torque. The role of the speed loop is to enable the vehicle to quickly respond to the change in the target folding angle.

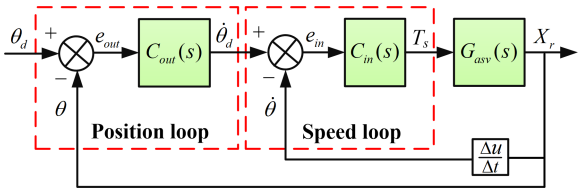

FIGURE 5. The structure of double closed-loop controller with folding position-speed.

Since the speed is related to the position, the controller adopts the form of a folding position loop and speed loop in series. The inner loop is the folding speed loop, and the outer loop is the folding position loop. The output of the previous loop is the input of the next loop, and the output of the last loop is the steering control amount T_s. The closed-loop control adopts the PID algorithm, then the inner and outer loop transfer functions are as follows:

$$C_{in}(s) = K_{p-in} + K_{i-in}\frac{1}{s} + K_{d-in}s \tag{27}$$

$$C_{out}(s) = K_{p-out} + K_{i-out}\frac{1}{s} + K_{d-out}s \tag{28}$$

Based on the dynamics model of ASVs and using a sinusoidal signal as input, PID parameters are determined through time domain analysis of the folding steering process. Among them, the frequency range of the sinusoidal signal from 0.1 Hz to 2 Hz, changing by 0.1 Hz at each step, the amplitude range from 0 deg to 30 deg, changing by 5 deg at each step, and the range of steering torque is set to be between -11600 N·m to 11600 N·m. Finally, the outer-loop parameters of the double closed-loop controller are specified as $K_{p-out} = 30000$, $K_{i-out} = 0$, $K_{d-out} = 20000$, and the inner loop adopts proportional control with a parameter $K_{p-in} = 5$.

Chopping refers to a signal processing technique where the steering demand torque signal is modulated to distinguish between components that are the same with and opposed to the direction of the folding motion. This chopping process is implemented through an amplitude limiting operation, denoted as:

$$\begin{cases} T_{sp} = T_s,\ T_{sn} = 0 & sign(T_s) = sign(\dot{\theta}_d) \\ T_{sp} = 0,\ T_{sn} = T_s & sign(T_s) \neq sign(\dot{\theta}_d) \end{cases} \tag{29}$$

where T_{sp} is the torque where the steering demand torque is in the same direction as the folding velocity, and T_{sn} is the torque where the steering demand torque is in the opposite direction to the folding velocity.

B. FOLDING STEERING TORQUE DISTRIBUTION BASED ON FREQUENCY DIVISION COOPERATION

Since the frequency domain characteristics depict the response capability of the system to various frequency input signals, the steering demand torque is allocated based on the frequency domain characteristics of both the differential steering system and the hydraulic steering system. Specifically, the respective target steering torques for the two

$$\begin{cases} \dot{p}_1 = E_1/V_1[q_1 - A_1\Delta\dot{X}_L + A_2\Delta\dot{X}_R - 2C_i(p_1 - p_2) - 2C_e p_1] \\ \dot{p}_2 = E_1/V_2[-q_2 - A_1\Delta\dot{X}_R + A_2\Delta\dot{X}_L + 2C_i(p_1 - p_2) + 2C_e p_2] \\ \quad i_c > 2.5\ ,\ \theta > 0 \quad \text{(Turn right)} \end{cases} \tag{23}$$

$$\begin{cases} \dot{p}_1 = E_1/V_2[q_1 - A_1\Delta\dot{X}_R + A_2\Delta\dot{X}_L - 2C_i(p_1 - p_2) - 2C_e p_1] \\ \dot{p}_2 = E_1/V_1[-q_2 - A_1\Delta\dot{X}_L + A_2\Delta\dot{X}_R + 2C_i(p_1 - p_2) + 2C_e p_2] \\ \quad i_c < -2.5,\ \theta < 0 \quad \text{(Turn left)} \end{cases} \tag{24}$$

$$\begin{cases} \dot{p}_1 = E_1/V_2[-A_1\Delta\dot{X}_R + A_2\Delta\dot{X}_L - 2C_i(p_1 - p_2) - 2C_e p_1] \\ \dot{p}_2 = E_1/V_1[-A_1\Delta\dot{X}_L + A_2\Delta\dot{X}_R + 2C_i(p_1 - p_2) + 2C_e p_2] \\ \quad -2.5 \leq\ i_c \leq 2.5,\ \theta = 0 \end{cases} \tag{25}$$

steering systems are derived through the frequency decomposition of the steering demand torque. In this manner, the two steering modes can be coordinated to avoid mutual interference. Furthermore, the steering demand torque after frequency decomposition represents the respective desired output of the two steering systems. However, these values cannot be directly employed as the control targets for the drive motor and hydraulic cylinder. Instead, they must be further transformed into the control inputs for each actuator through the differential torque distribution model and the reverse solution model of hydraulic pressure.

1) HIGH-LOW FREQUENCY DYNAMIC DISTRIBUTION MODEL

In the steering control process of ASVs, the steering demand torque is composed of components of different frequencies.

Among them, the high-frequency component contains the rapid changes or details of the signal, and the low-frequency component represents the overall trend or smooth part of the signal. In this paper, the frequency domain characteristics of the differential steering system and hydraulic steering system are utilized to assign steering demand torque, specifically by employing filtering technology to decompose the frequency components of the steering demand torque.

The first-order low-pass filtering algorithm is a classical signal processing technology with a simple structure, fast calculation speed, and stable filtering effect [28], [29]. Therefore, based on the first-order low-pass filtering algorithm, this study designed the high-low frequency dynamic distribution model of the frequency division cooperative steering control strategy. The working principle is to calculate the current filter output value through the weighted average of the current sampling value and the previous filter output value. Therefore, the positive torque T_{sp} in the vehicle steering demand torque is taken as the input, and it is divided into high-frequency torque T_{sp_h} and low-frequency torque T_{sp_l}, expressed as:

$$\begin{cases} T_{sp\_l}(t) = aT_{sp}(t) + (1-a)\,T_{sp\_l}(t-1) \\ T_{sp\_h}(t) = T_{sp}(t) - T_{sp\_l}(t) \end{cases} \tag{30}$$

where $T_{sp}(t)$ is the sampling value of the filter, $T_{sp\_l}(t-1)$ is the filtering result of the previous moment, and a is the filtering coefficient, between 0 to 1, which determines the filtering effect of the algorithm, expressed as:

$$a = \frac{1}{1 + \frac{f}{2\pi f_H}} \tag{31}$$

where f is the sampling frequency, and f_H is the cut-off frequency.

2) DIFFERENTIAL TORQUE DISTRIBUTION MODEL

The torque distribution algorithm of distributed-drive vehicles to achieve differential steering is primarily categorized into two types: rule-based and optimization-based [30], [31]. Although the optimization-based torque distribution algorithm offers potential advantages, it tends to be more complex and exhibits poorer real-time performance. Consequently, the rule-based torque distribution algorithm is adopted. Since the yaw movement direction of the front body and rear body for the ASVs is opposite when steering, the relationship between the differential steering torque of the front body and rear body and the high-frequency torque T_{sp_h} and negative torque T_{sn} is as follows:

$$\begin{cases} M_{txf} = T_{sp\_h} + T_{sn} \\ M_{txr} = -(T_{sp\_h} + T_{sn}) \end{cases} \tag{32}$$

To reduce the sensitivity of the differential folding steering system to the disturbance with high frequency and tiny amplitude, further restrictions need to be imposed on the upper bound of the frequency response of differential steering torque M_{txf} and M_{txr}. The restriction method still adopts the low-pass filter in equation (30), where the filter coefficient is calibrated according to the driving experience in real vehicle applications. The relationship between differential steering torque and wheel force is as follows:

$$\begin{cases} M_{txf} = (F_{x1} - F_{x2})B = 2\Delta F_{txf}B \\ M_{txr} = (F_{x3} - F_{x4})B = 2\Delta F_{txr}B \end{cases} \tag{33}$$

Therefore, the amounts of torque variation required by the front and rear drive motors to achieve differential steering are:

$$\begin{cases} \Delta T_f = \dfrac{M_{txf}}{2Bi_0}r \\ \Delta T_r = \dfrac{M_{txr}}{2Bi_0}r \end{cases} \tag{34}$$

To ensure the vehicle speed does not change greatly after applying the differential torque, the driving torque of the whole vehicle needs to remain unchanged. Therefore, during the differential steering process, when the driving torque on one side of the body increases, the driving torque on the other side should be reduced to ensure the total driving torque of the same axle remains unchanged. The target output torque of each drive motor is as follows:

$$\begin{cases} T_{m1} = T_{df} + \dfrac{T_{sp\_h} + T_{sn}}{2Bi_0}r \\ T_{m2} = T_{df} - \dfrac{T_{sp\_h} + T_{sn}}{2Bi_0}r \\ T_{m3} = T_{dr} - \dfrac{T_{sp\_h} + T_{sn}}{2Bi_0}r \\ T_{m4} = T_{dr} + \dfrac{T_{sp\_h} + T_{sn}}{2Bi_0}r \end{cases} \tag{35}$$

where T_{di} is the drive torque to maintain the vehicle speed, $i \in (f, r)$.

3) HYDRAULIC PRESSURE REVERSE SOLUTION MODEL

The relationship between the hydraulic steering torque at the center of mass for the front and rear bodies and the low-frequency steering torque T_{sp_l} is:

$$\begin{cases} M_{sf} = T_{sp\_l} \\ M_{sr} = -T_{sp\_l} \end{cases} \tag{36}$$

According to the force relationship (6) of the articulated structure in Part A of Section II, the relationship between the hydraulic cylinder thrust and the torque acting on the center of mass of the front and rear bodies is equation (37), as shown at the bottom of the page, then the hydraulic cylinder thrust is shown in equation (38), as shown at the bottom of the page.

According to the dynamic model of the hydraulic steering system in Part C of Section II, the force balance equation of the hydraulic cylinder is as follows:

$$\begin{cases} F_{hL} = A_1 P_{L1} - A_2 P_{L2} - f_{s1}\Delta\dot{X}_L \\ F_{hR} = A_1 P_{R1} - A_2 P_{R2} - f_{s1}\Delta\dot{X}_R \end{cases} \tag{39}$$

Define the pressure relationship in each chamber of the hydraulic cylinder as:

$$\begin{cases} P' = P_{L1} = P_{R2} \\ P'' = P_{R1} = P_{L2} \end{cases} \tag{40}$$

By reverse solving (38) to (40), the relationship between the target pressure of the hydraulic cylinder and the low-frequency steering torque during steering can be obtained as follows:

$$\begin{cases} P' = \dfrac{f_{s1}(A_1\Delta\dot{X}_L + A_2\Delta\dot{X}_R) + F_{hL}A_1 + F_{hR}A_2}{A_1^2 - A_2^2} \\ P'' = \dfrac{f_{s1}(A_1\Delta\dot{X}_R + A_2\Delta\dot{X}_L) + F_{hR}A_1 + F_{hL}A_2}{A_1^2 - A_2^2} \end{cases} \tag{41}$$

C. FILTER COEFFICIENT DETERMINATION BASED ON FREQUENCY DOMAIN ANALYSIS

When the sampling frequency has been determined, according to the filter coefficient formula (31), a higher cut-off frequency results in a larger filter coefficient a, which increases the weight of the current input, enhancing the tracking effect on the input and reducing amplitude attenuation. Conversely, a lower cut-off frequency leads to a smaller filter coefficient a, making the filtering effect more pronounced and causing amplitude attenuation, as high-frequency components are more effectively suppressed. Given the critical role of the cut-off frequency, it is essential to determine it in the design of the filter. In this study, the frequency characteristics of the differential steering system and hydraulic steering system are used to determine the cut-off frequency. The transfer functions of two steering systems are established and analyzed as follows.

1) DIFFERENTIAL STEERING SYSTEM

The differential steering system primarily relies on the electric wheels on both sides of the vehicle body to output different longitudinal forces to achieve vehicle steering. Therefore, the motor adopts the torque control method. From the working characteristics of the motor, it can be seen that there is a certain response hysteresis, arising from both the processing of the motor controller and the transition from the input regulation voltage to the torque output, resulting in a delay from the target torque to the actual torque response. Assuming that the motor output torque follows the target torque well, and the target torque does not exceed the limitations of the motor characteristics, then the relationship between the target torque T_{target} and the actual output T_m of the motor can be equivalent to a first-order inertia system [32], as follows:

$$T_m = \frac{k}{t_m s + 1} T_{target}\eta_m \tag{42}$$

where k is the proportional constant, here is 1, t_m is the time constant of the motor response, and η_m is motor efficiency.

According to the differential equation of wheel rotation dynamics (9), ignoring the rolling resistance of the wheel and assuming the vehicle is running in a steady state, i.e., the angular acceleration of wheel rotation $\dot{\omega} = 0$, the longitudinal force of the wheel is expressed as:

$$F_{xi} = \frac{T_{mi} i_0 \eta_t}{r_w} \tag{43}$$

When the driving force of the wheels on both sides of the vehicle body is unequal, a differential torque will be generated at the center of the axle, and eventually transferred to the center of mass of the vehicle body. Therefore, the maximum differential steering torque formed by unequal wheel forces from the left and right wheels is expressed as:

$$T_s = (F_{x1} - F_{x2})B \approx 2F_{x1}B \tag{44}$$

Based on (42) to (44), the closed-loop transfer function of a differential steering system with motor target torque T_{target} as input and steering torque T_s as output is as follows:

$$M(s) = \frac{2Bi_0\eta_t\eta_m k}{r_w t_m s + r_w + 2Bi_0\eta_t\eta_m k} \tag{45}$$

2) HYDRAULIC STEERING SYSTEM

The principle of the hydraulic steering system controlled by an electro-hydraulic proportional valve is shown in Fig. 6.

$$\begin{cases} M_{sf} = (F_{hL}\cos\alpha_1 - F_{hR}\cos\alpha_2)c + (F_{hR}\sin\alpha_2 - F_{hL}\sin\alpha_1)L_{f3} \\ M_{sr} = (F_{hR}\cos\alpha_4 - F_{hL}\cos\alpha_3)d + (F_{hR}\sin\alpha_4 - F_{hL}\sin\alpha_3)L_{r3} \end{cases} \tag{37}$$

$$\begin{cases} F_{hL} = \dfrac{T_{sp\_l}[(d\cos\alpha_4 + L_{r3}\sin\alpha_4) + (L_{f3}\sin\alpha_2 - c\cos\alpha_2)]}{(c\cos\alpha_1 - L_{f3}\sin\alpha_1)(d\cos\alpha_4 + L_{r3}\sin\alpha_4) + (d\cos\alpha_3 + L_{r3}\sin\alpha_3)(L_{f3}\sin\alpha_2 - c\cos\alpha_2)} \\ F_{hR} = \dfrac{T_{sp\_l}[(d\cos\alpha_3 + L_{r3}\sin\alpha_3) - (c\cos\alpha_1 - L_{f3}\sin\alpha_1)]}{(L_{f3}\sin\alpha_2 - c\cos\alpha_2)(d\cos\alpha_3 + L_{r3}\sin\alpha_3) + (d\cos\alpha_4 + L_{r3}\sin\alpha_4)(c\cos\alpha_1 - L_{f3}\sin\alpha_1)} \end{cases} \tag{38}$$

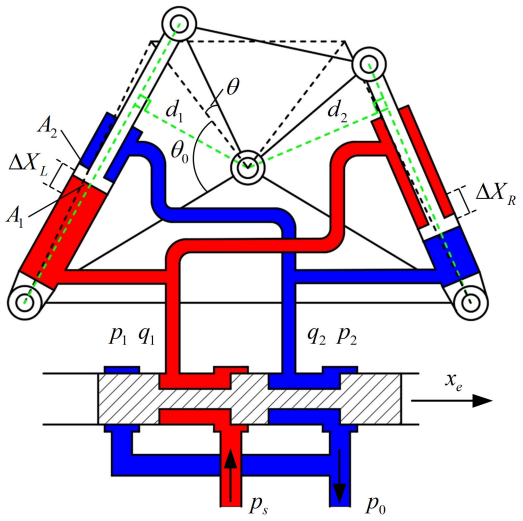

FIGURE 6. Hydraulic steering system of electro-hydraulic proportional valve controlled.

Taking the state of the vehicle turning to the right as an example, the hydraulic steering system model is simplified to obtain the system transfer function.

Within the effective stroke of the valve spool, the electromagnetic force of the proportional solenoid valve is approximately proportional to the input current i_c. Therefore, the dynamic equation of the spool is as follows:

$$K_i i_c = m_e \frac{d^2 x_e}{dt^2} + C_e \frac{dx_e}{dt} + 2K_e x_e \tag{46}$$

where m_e is the equivalent mass of the valve spool, x_e is the displacement of the valve spool, K_e is the spring stiffness, C_e is the viscous damping coefficient, and K_i is the force-current amplification coefficient of the proportional solenoid.

When the vehicle turns right, $x_e > 0$, $p_1 > p_2$, the load flow equation of the electro-hydraulic proportional direction valve is:

$$q_1 = C_d w x_e \sqrt{\frac{2}{\rho}(p_s - p_1)} \tag{47}$$

$$q_2 = C_d w x_e \sqrt{\frac{2}{\rho} p_2} \tag{48}$$

Since the steering system is composed of two hydraulic cylinders in parallel, the oil volume of the hydraulic cylinder contains two parts, expressed as:

$$V_1 = V_{OL1} + A_1 \Delta X_L + V_{OR2} - A_2 \Delta X_R \tag{49}$$

$$V_2 = V_{OL2} - A_2 \Delta X_L + V_{OR1} + A_1 \Delta X_R \tag{50}$$

where V_1 is the volume of the left rodless chamber and the right rodded chamber, V_2 is the volume of the right rodless chamber and the left rodded chamber, V_{OL1}, V_{OL2} and V_{OR1}, V_{OR2} are the initial volumes of the rodless and rodded chamber of the left and right hydraulic cylinders, respectively. Then the flow continuity equation of the hydraulic cylinder is as follows:

$$q_1 = A_1 \frac{d\Delta X_L}{dt} - A_2 \frac{d\Delta X_R}{dt} + 2C_i(p_1 - p_2) + 2C_e p_1 + \lambda_1 \frac{dp_1}{dt} \tag{51}$$

$$q_2 = A_1 \frac{d\Delta X_R}{dt} - A_2 \frac{d\Delta X_L}{dt} + 2C_i(p_1 - p_2) - 2C_e p_2 - \lambda_2 \frac{dp_2}{dt} \tag{52}$$

where $\lambda_1 \approx (V_{OL1} + V_{OR2})/E_1$, $\lambda_2 \approx (V_{OL2} + V_{OR1})/E_1$.

Define p_L and q_L denote the load pressure and load flow, respectively. According to the power balance principle can be obtained:

$$p_L \times q_L = p_1 q_1 - p_2 q_2 = (p_1 - n p_2)\, q_1 \tag{53}$$

Then define:

$$p_L = p_1 - n p_2 \tag{54}$$

$$q_L = q_1 \tag{55}$$

Combining (47) and (48), $q_2/q_1 \approx A_2/A_1 = n$, then obtain:

$$p_2 = (p_s - p_1) n^2 \tag{56}$$

By eliminating p_1 or p_2 from (56) and (54), then obtain:

$$\begin{cases} p_1 = \dfrac{n^3 p_s + p_L}{1 + n^3} \\ p_2 = \dfrac{n^2 (p_s - p_L)}{1 + n^3} \end{cases} \tag{57}$$

Based on (55) and (57), linearizing (47) at any working point (p_{La}, x_{ea}) is obtained:

$$q_L = K_q x_e - K_c p_L \tag{58}$$

where

$$K_q = C_d w \sqrt{\frac{2}{\rho}\left(\frac{p_s - p_{La}}{1 + n^3}\right)}$$

is the flow amplification coefficient, and

$$K_c = \frac{C_d w x_{ea}}{2(p_s - p_{La})} \sqrt{\frac{2}{\rho}\left(\frac{p_s - p_{La}}{1 + n^3}\right)}$$

is the flow-pressure amplification coefficient.

Based on (51) and combined with (55) to (57), obtained:

$$q_L = A_1 \frac{d\Delta X_L}{dt} - A_2 \frac{d\Delta X_R}{dt} + C_{i1} p_L + C_{e1} p_s + \lambda_{11} \frac{dp_L}{dt} \tag{59}$$

where

$$\lambda_{11} = \frac{\lambda_1}{1 + n^3} = \frac{1}{1 + n^3}\left(\frac{V_{01L} + V_{02R}}{E_1}\right),$$

$$C_{e1} = \frac{2C_i(n^3 - n^2) + 2C_e n^3}{1 + n^3}, \; C_{i1} = \frac{2C_i(1 + n^2) + 2C_e}{1 + n^3}.$$

Laplace transform is performed on (46), (58), and (59), as:

$$K_i I = m_e s^2 X_e + C_e s X_e + 2K_e X_e \tag{60}$$

$$Q_L = K_q X_e - K_c P_L \tag{61}$$

$$Q_L = A_1 s \Delta X_L - A_2 s \Delta X_R + C_{i1} P_L + C_{e1} P_s + \lambda_{11} s P_L \tag{62}$$

Based on (60), the transfer function of the electro-hydraulic proportional directional valve is as follows:

$$G(s) = \frac{X_e}{I} = \frac{K_i}{m_e s^2 + C_e s + 2K_e} \tag{63}$$

By combining (61) and (62), eliminating intermediate variables Q_L, and ignoring internal and external leakage coefficient, the system transfer function with spool displacement X_e as input and P_L as output is obtained as:

$$H(s) = \frac{K_q}{\lambda_{11} s + K_c} = \frac{K_q}{\frac{1}{1+n^3}\left[\frac{\pi D^2}{4}(l_1 + l_2)\frac{1}{E_1} + \frac{V_{01L}+V_{02R}}{E_1}\right] s + K_c} \tag{64}$$

To facilitate calculation, assuming that the length of the steering arm in the hydraulic steering system is constant and equal to $d_0 = d_1 = d_2$, the closed-loop transfer function of the hydraulic steering system with the spool control current i_c as input and the steering torque T_s as output is as follows:

$$C(s) = \frac{G(s)H(s)(A_1 + A_2)d_0}{1 + G(s)H(s)(A_1 + A_2)d_0} \tag{65}$$

Fig. 7 shows closed-loop Bode diagrams for differential and hydraulic steering systems. Among them, the pressure of the hydraulic system is 5 MPa, and assuming that the load pressure of the light load condition is 1 MPa, and the load pressure of the heavy load condition is 4 MPa. It can be seen that the closed-loop cutoff frequency of the differential steering system is 66.6 Hz, and that of the hydraulic steering system under light and heavy load conditions is 14.5 Hz and 11.4 Hz, respectively. Obviously, the system bandwidth of the differential steering system is higher. When the amplitude decays to -3 dB, the phase delay of the differential steering system is 44.6 deg, and that of the hydraulic steering system under light and heavy load conditions is 151.2 deg and 131.4 deg, respectively. Therefore, under the same amplitude ratio, the phase delay of the differential steering system is the smallest and has higher real-time performance. From the phase-frequency characteristic curve, it can be seen that around 0.3 Hz, the hydraulic steering system and the differential steering system begin to show an obvious phase delay phenomenon, and the phase delay trend of the hydraulic steering system under heavy load conditions is the largest. To make full use of the rapid response ability of differential steering system and reduce the impact of bandwidth limitation of hydraulic steering system on folding steering performance, the turning point of phase delay of the hydraulic steering system is determined as the cutoff frequency of first-order low-pass filtering algorithm, i.e., $f_H = 0.3$ Hz, the filtering coefficient $a = 0.018$.

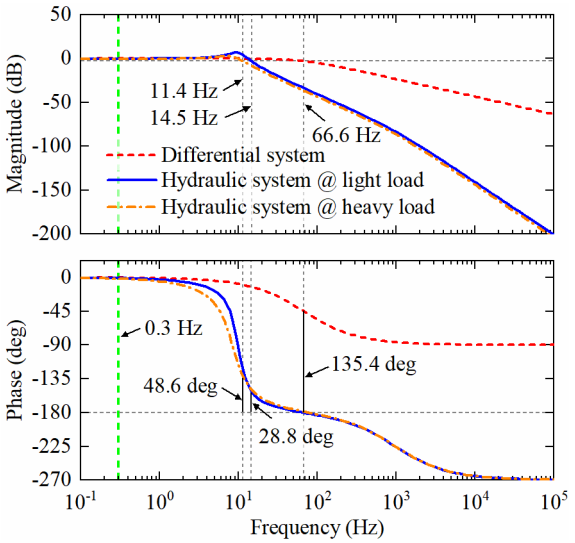

FIGURE 7. Closed-loop Bode diagrams for differential and hydraulic steering systems.

IV. CASE STUDY

To verify the effectiveness of the proposed folding steering control method based on the differential-hydraulic frequency division cooperation (CSC), a numerical simulation model is established in MATLAB/Simulink, based on the verified dynamic model of the DASVs, as shown in Fig. 8. The comparison object is the hydraulic steering control (HSC).

A. SIMULATION MODEL ESTABLISHMENT AND VERIFICATION

To ensure the credibility of the performance analysis results of the folding steering control, the simulation model is first verified based on real-vehicle experiments. In the validation scheme, the actual driving signals recorded during the real-vehicle experiments, such as vehicle speed and steering angle, are utilized as inputs to the numerical simulation model. This ensures that the simulation environment is approximately consistent with the experimental conditions. By comparing the experimental and simulation data of key vehicle state parameters in the time domain, the accuracy of the simulation model is verified, and the key parameters in the simulation model are corrected according to the analysis results.

The experimental vehicle is a scale prototype of the mine underground support handling vehicle, which adopts the drive and control systems of the real vehicle, as well as the four-wheel-drive form of the motor plus reducer combination, as shown in Fig. 9. To detect the vehicle state information during the experiment, the vehicle is also equipped with the wheel speed encoder, angle sensor, displacement sensor, and an integrated navigation system. And the acquisition system consists of the bus test software (Vehicle Spy3) and the CAN data acquisition module (ValueCAN3), which can record the data from each sensor and the vehicle control system in real time. The main parameters of the experimental vehicle are listed in Table 1.

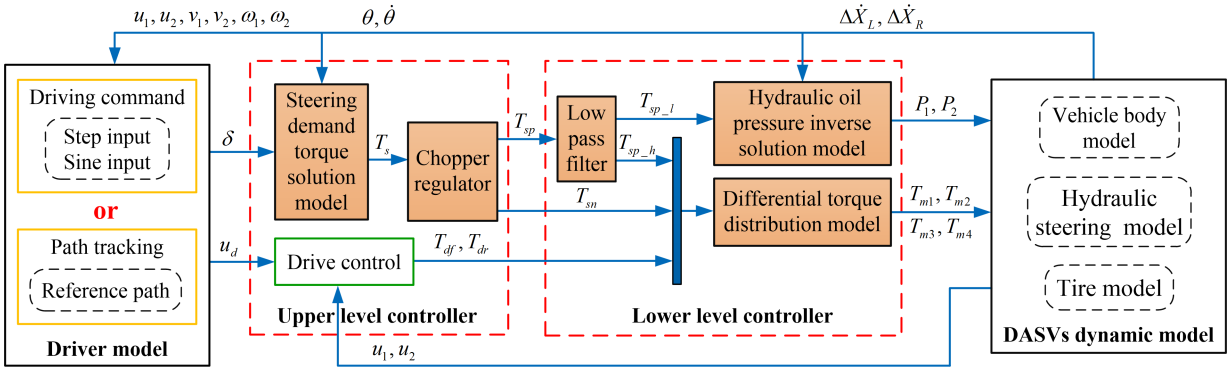

FIGURE 8. Simulation model of folding steering control strategy.

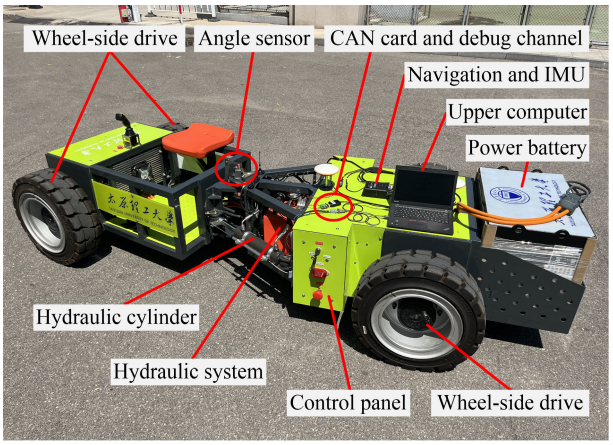

FIGURE 9. Experimental vehicle and sensor layout (Angle sensor: SME-64, 0-360 deg @ 0.08 deg, Linear displacement sensor: KPM18-300, 0-300 mm @ 0.01 mm, Integrated Navigation System: CSL-410, attitude ± 400 deg, acceleration ± 8g).

TABLE 1. The main parameters of the experimental vehicle.

Parameters	Value	Unit
Front body mass with unload	570	kg
Front body mass with full load	1570	kg
Rear body mass	1350	kg
Moment of inertia for front body at unload	164.9	kg·m^2
Moment of inertia for front body at full load	409.4	kg·m^2
Moment of inertia for rear body	529.8	kg·m^2
Rolling radius	0.34	m
Rolling resistance coefficient	0.02	-
Maximal articulation angle	35	deg
Wheel track	1.16	m
Rated torque of drive motor	92.5	N·m
Gear ratio of the wheel reducer	64	-
Longitudinal tire stiffness	115000	N·m^{-1}
Lateral tire stiffness	57000	N·rad^{-1}

The experiment employs full-load transient steering condition, i.e., when the vehicle is driving at a constant speed, the folding angle changes continuously from one value to another. The experimental site is a single-shift line path arranged with conical barrels, in which the longitudinal length is 10 m and the lateral length is 5 m of the lane change section. During the experiment, first drive the vehicle to accelerate from a standstill to 10 km/h, and then maintain a constant speed. When reaching the lane change section, the steering lever is operated to make the vehicle shift to the left to the straight lane on the other side. Fig. 10 shows the experimental scene, as well as the driving signals about vehicle speed and steering angle.

Fig. 11 shows the comparison of the vehicle parameters between the simulation and experiment. As shown in Fig. 11(a), both experimental and simulated values of the folding angle closely track the changes in the steering control target. Notably, the folding angle attains its maximum values for left and right turns approximately at 11.5s and 13.5s, respectively, which is consistent with the steering control inputs. In Fig. 11(b), the variation in vehicle speed is presented. Apart from a relatively minor amplitude deviation observed during the steering process, the simulated vehicle speed can follow the experimental speed trend and remains stable at approximately 10 km/h. Combining the changes in the yaw velocity of the front and rear bodies in Fig. 11(c) and Fig.11(d), it can be seen that the simulation results are largely congruent with the experimental results. Notably, during the steering process, the simulation also shows the oscillation phenomenon of the steering system, which arises from the compression of oil in the hydraulic cylinder, due to the instability of the steering lever and the inertia movement of the counterweight.

Fig. 12 shows the comparison between the actual vehicle trajectory and the simulated trajectory. During the steering process, the lateral movement distance of the vehicle is about 4 m, and the longitudinal distance is about 10 m, which conforms to the experimental scheme. Moreover, the trajectory variation trend of the simulation is consistent with that of the actual vehicle. The maximum trajectory deviation of the front and rear body occurs at the lateral displacement in the

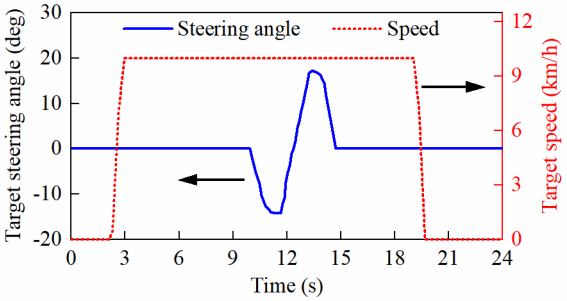

(a) Driving signals

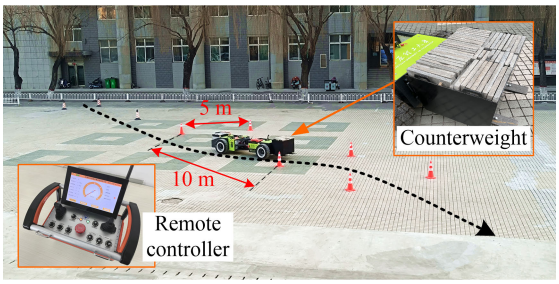

(b) Experimental scene

FIGURE 10. Experiment process of full load transient steering condition.

process of lane change, and the deviation values are 0.19 m and 0.26 m, respectively. Based on the above analysis, it can be observed that the variation trend of vehicle state parameters and motion trajectory in the DASVs model established in this study is consistent with experimental results, with smaller deviation values. Therefore, the model possesses high credibility and can be utilized for subsequent folding control and path tracking control analyses.

B. STEERING CONTROL PERFORMANCE ANALYSIS

To analyze the folding follow-up performance of the CSC, simulations were conducted using step inputs of continuous steering angle with steady-state values of 5 deg, 10 deg, and 15 deg, as well as sinusoidal inputs of steering angle with amplitudes of 10 deg, 20 deg, and 30 deg, and a frequency of 0.8 Hz. These simulations were performed on a good road surface, at a speed of 10 km/h, and under unloaded conditions. The results are presented in Fig. 13 and 14.

As can be seen from Fig. 13(a), there is no overshoot or oscillation in the folding angle of CSC and HSC, therefore, the steering control system is relatively stable. Moreover, under the continuous step input of 5 deg, 10 deg, and 15 deg, the average rise time of folding angle for CSC is 0.789s, 0.766s, and 0.863s, and for HSC is 0.998s, 1.006s, and 1.014s, respectively. Compared with HSC, CSC has a 20.9%, 23.9%, and 14.9% reduction in folding angle rise time, respectively, which enables fast tracking of steady-state steering targets. It is worth noting that, at t=10s, the tangent slopes of the response curves for the CSC are 36.4, 48.6, and, 56.9, and for the HSC are 9.4, 18.3, and 26.5, respectively. The intervention of the differential torque at the initial

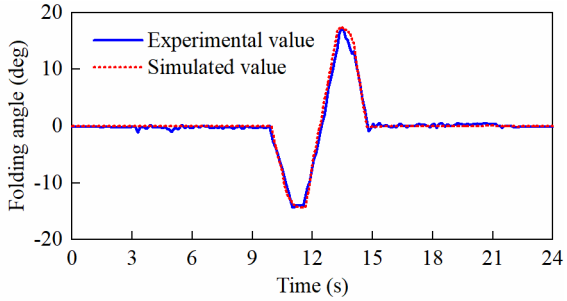

(a) Folding angle

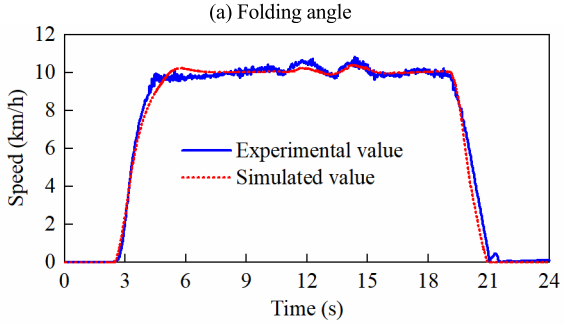

(b) Vehicle speed

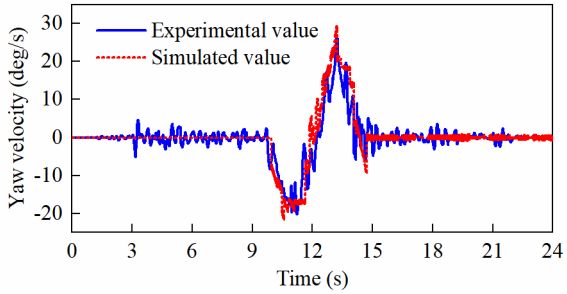

(c) Yaw velocity of the front body

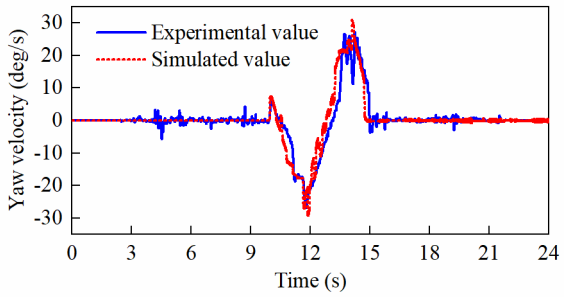

(d) Yaw velocity of the rear body

FIGURE 11. Comparison of vehicle state parameters.

steering moment makes the folding response of the CSC faster. Fig. 13(b) shows the control results during the step steering at every 10 deg interval. It can be seen that the total steering demand torque shows a sudden change at the initial steering moment, then slowly decreases, and finally stays near a stable value to maintain the steady steering process. This is because the vehicle must overcome a large body inertia of mass when transitioning from steady-state driving to transient steering, which requires a large and rapid response in steering torque to ensure prompt steering action. Compared

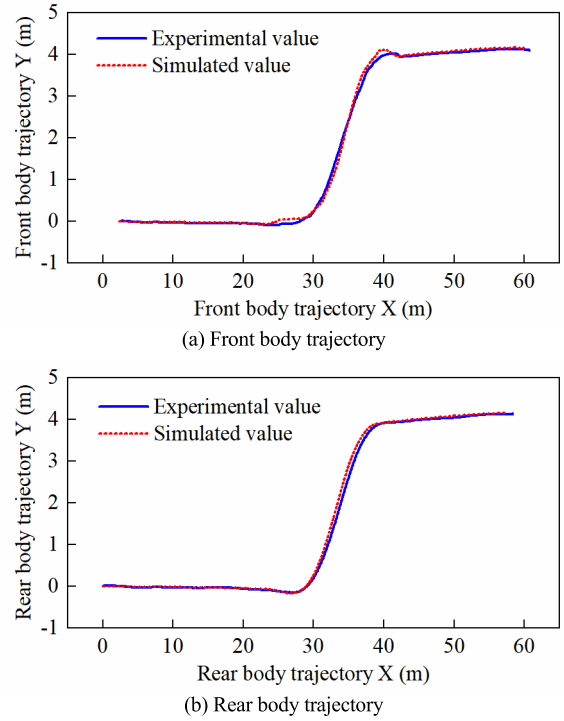

(a) Front body trajectory

(b) Rear body trajectory

FIGURE 12. Comparison of vehicle trajectories.

with HSC, the rapid response of motor torque in the CSC is fully utilized at the initial steering moment, so that the folding angle of CSC can quickly follow the desired steering angle. In combination with Fig. 13(c), the variation of vehicle speed for CSC has a more obvious fluctuation, but the overall fluctuation amplitude is smaller, staying within 1 km/h. However, for ASVs with low driving speed and complex operating conditions, the improvement of steering performance is more important than driving.

As shown in Fig. 14(a), under the sinusoidal input of the steering angle with amplitudes of 10 deg, 20 deg, and 30 deg, the average amplitude ratios of the folding angle for CSC are 1.005, 0.998, and 1.014, and the average phase delays are 3.8 deg, 4 deg, and 4.7 deg, respectively. The average amplitude ratios of HSC are 0.963, 0.968, and 0.971, and the average phase delays are all 7.5 deg. In contrast, the phase delay of CSC is reduced by 49.6%, 46.2%, and 37.7%, respectively, and the lag time and amplitude difference are smaller, which has better transient following performance. Fig. 14(b) shows the control result of the sinusoidal input with an amplitude of 10 deg. It can be seen that the differential steering system can always provide a certain steering torque at the moment of each reversal, which slows down the impact of the hydraulic system during the reversal process, resulting in the yaw velocity of the front and rear bodies smoother, and ensures better stability during the steering process of the vehicle. Fig. 14(c) shows the vehicle speed variation of the sinusoidal input with an amplitude of 10 deg. The speed fluctuation amplitude of the two steering systems is kept in a small range. According to the above analysis, the folding

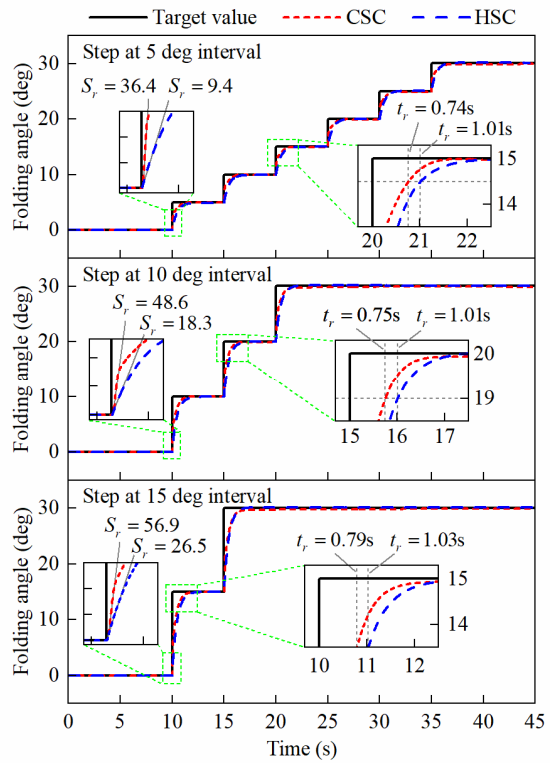

(a) Response of folding angle under step input

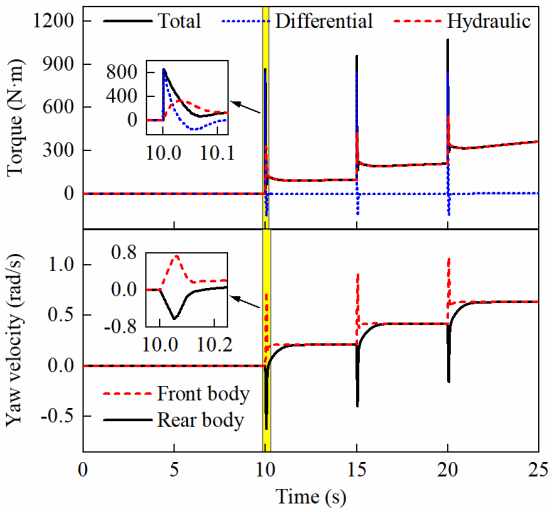

(b) Control results during the step steering at every 10 deg interval

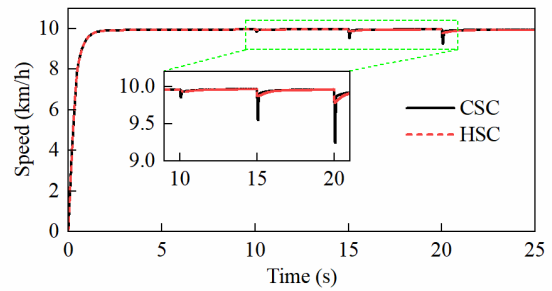

(c) Variation of vehicle speed during the step steering at every 10 deg interval

FIGURE 13. Response comparison of step input for steering angle.

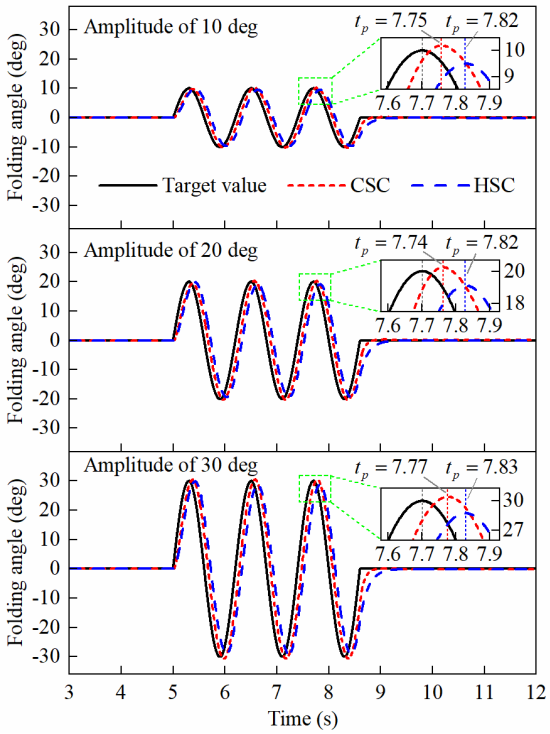

(a) Response of folding angle under sinusoidal input

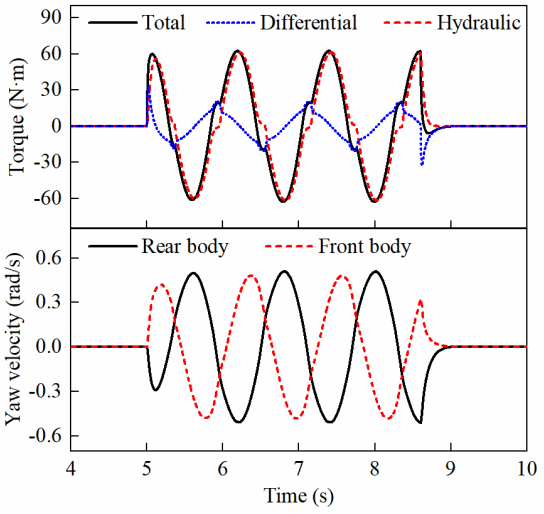

(b) Control results during the sinusoidal steering with an amplitude of 10 deg

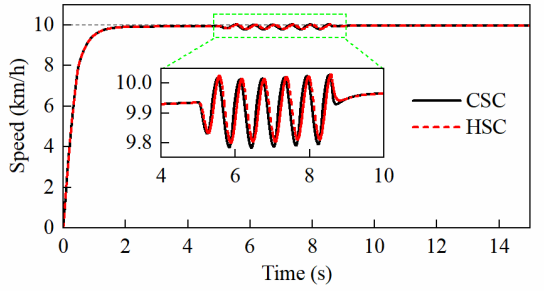

(c) Variation of vehicle speed during the sinusoidal steering with an amplitude of 10 deg

FIGURE 14. Response comparison of sinusoidal input for steering angle.

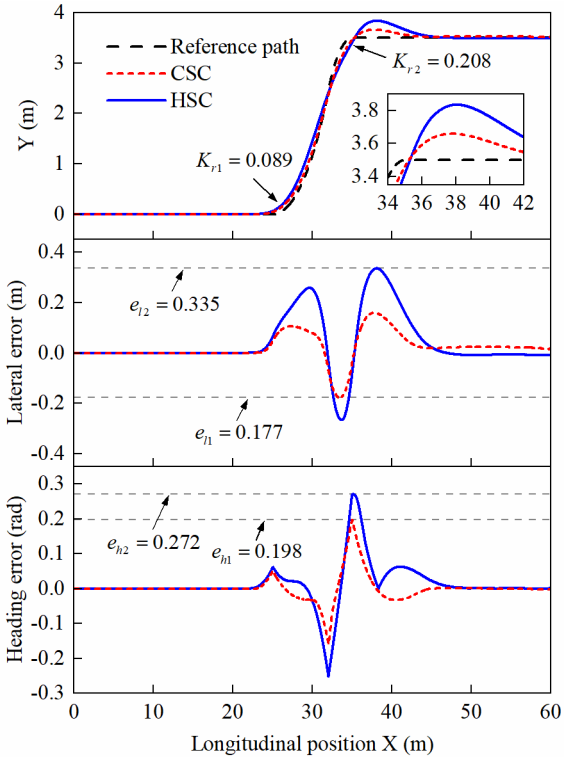

FIGURE 15. Single-shift line path tracing results.

steering system based on CSC has better steady state and transient control effects.

C. PATH TRACKING PERFORMANCE ANALYSIS

Being able to execute steering control commands accurately, stably, and rapidly is an important foundation for achieving unmanned autonomous driving [33]. In this section, a path-tracking controller for ASVs based on PurePursit is established according to reference [34], and path-tracking performance under both CSC and HSC are compared and analyzed, respectively.

Typical reference paths for path tracking tests include straight line, ring, snake, and single-shift line paths, etc. Among them, the single-shift line path contains the characteristics of both straight-line driving and left and right turns [35]. Therefore, the test condition utilizes a single-shift line path with a vehicle speed of 10 km/h under full load. The results are shown in Fig. 15. Overall, the path tracking error appears at the turn, and the tracking error at the second turn is significantly larger than that at the first turn, which is due to the greater curvature at the second turn. Specifically, the peak lateral error of HSC is 0.335 m and the peak heading angle error is 0.272 rad, whereas for CSC is 0.177 m and 0.198 rad, respectively. By comparison, the maximum lateral error and heading angle error of CSC are reduced by 47.2% and 27.2%, respectively, which shows that CSC can improve

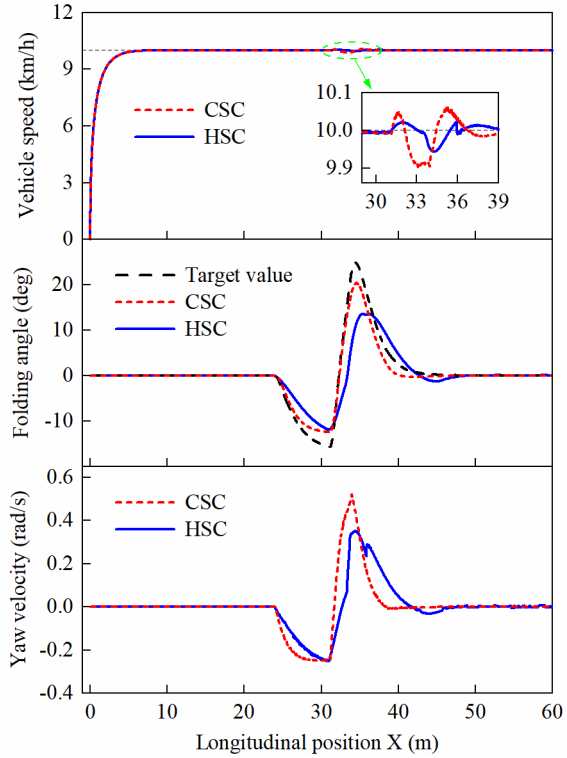

FIGURE 16. Vehicle motion state parameters.

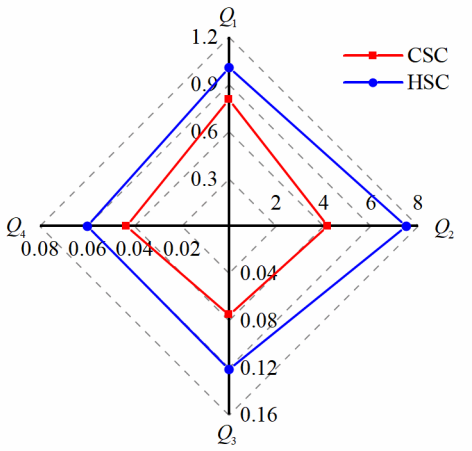

FIGURE 17. Comprehensive performance comparison.

TABLE 2. Evaluation indicators.

Indicator	Computational formula
Folding angle rise time	$Q_1 = (t_{r,5} + t_{r,10} + t_{r,15})/3$
Folding angle delay time	$Q_2 = (t_{d,10} + t_{d,20} + t_{d,30})/3$
Lateral position error	$Q_3 = \sum_1^N e_{li}/N$
Heading angle error	$Q_4 = \sum_1^N e_{hi}/N$

path-tracking accuracy. Moreover, CSC can make the vehicle enter the stable state earlier at the end of the turning, indicating that the vehicle returns to the right direction faster under the cooperative steering.

At the same time, according to the vehicle state parameters shown in Fig. 16, it can be seen that both CSC and HSC can effectively maintain the vehicle speed at the reference level. Although the speed fluctuations of CSC are relatively pronounced, the overall variation amplitude remains minimal ($\pm$0.1 km/h), which does not have a significant impact on vehicle driving. Furthermore, the changes in yaw velocity and folding angle are relatively smooth, and the changing trends of both are basically similar. From the above analysis, it can be seen that the path-tracking performance of DASVs utilizing CSC is superior to that achieved with HSC, i.e., different chassis steering-by-wire systems have a significant impact on the path-tracking performance. Specifically, if the folding pro-cess can be completed quickly and accurately, tracking deviation due to folding errors will be reduced, and conversely, the path tracking deviation will be increased.

Fig. 17 presents a radar chart that visually compares the performance of the folding control system. In this chart, smaller values along each axis indicate superior performance in the corresponding aspect. The evaluation indexes use the average folding angle rise time and delay time, both of which represent the folding performance, and the average lateral position error and heading angle error, both of which represent the path tracking performance, as shown in Table 2. Compared with HSC, CSC reduces the average rise time, delay time, lateral position error, and heading angle error by 19.8%, 44.4%, 38.1%, and 27.5%, respectively. Therefore, the comprehensive performance of CSC is significantly better than that of HSC, especially the delay time of folding angle has been greatly improved, and has better folding follow-up performance.

V. CONCLUSION

This paper introduces a novel control method for folding steering based on differential and hydraulic frequency division cooperation. Specifically, a double closed-loop control of folding angle and folding velocity is employed to determine the folding steering demand torque. Utilizing a first-order low-pass filtering algorithm, the steering demand torque is decomposed into high-frequency and low-frequency components, which are then allocated to the differential and hydraulic systems, respectively. Based on the experimentally verified articulated steering vehicle model and the PurePursit path tracking control algorithm, the performance of the proposed folding motion control method and its implication on path tracking accuracy are analyzed. The main conclusions are as follows:

1) The folding process of articulated steering vehicles can be decoupled from the overall vehicle steering process, enabling separate research to be conducted on the folding control process and improving the dynamic responsiveness of vehicle steering by optimizing the folding motion performance.

2) Frequency division cooperation can make full use of the respective advantages of the differential steering system and the hydraulic steering system, effectively improve the follow-up performance of the folding steering process, and avoid conflicts and interference between different steering actuators.

3) Folding motion control has a significant impact on the path-tracking performance of articulated steering vehicles, offering novel insights and guidance for enhancing the overall path-tracking control performance of these vehicles.

REFERENCES

[1] T. Xu, W. Fan, Y. Sun, X. Ji, and Y. Liu, "Differential steering control based on CNF and ADRC techniques for distributed-drive articulated heavy vehicles," *IEEE Trans. Veh. Technol.*, vol. 73, no. 5, pp. 6429–6442, May 2024.

[2] Q. Gu, G. Bai, G. Wang, Y. Meng, and L. Liu, "3D search based hybrid optimal trajectory planning for autonomous LHD in turning maneuvers," *IEEE Trans. Intell. Transp. Syst.*, vol. 23, no. 10, pp. 17704–17716, Oct. 2022.

[3] Y. Gao, Y. Ai, B. Tian, L. Chen, J. Wang, D. Cao, and F.-Y. Wang, "Parallel end-to-end autonomous mining: An IoT-oriented approach," *IEEE Internet Things J.*, vol. 7, no. 2, pp. 1011–1023, Feb. 2020.

[4] T. Lei, J. Wang, and Z. Yao, "Modelling and stability analysis of articulated vehicles," *Appl. Sci.*, vol. 11, no. 8, p. 3663, Apr. 2021.

[5] L. G. Dekker, J. A. Marshall, and J. Larsson, "Experiments in feedback linearized iterative learning-based path following for center-articulated industrial vehicles," *J. Field Robot.*, vol. 36, no. 5, pp. 955–972, Aug. 2019.

[6] F. Yang, X. Cao, T. Xu, and X. Ji, "A skid-steering method for path-following control of distributed-drive articulated heavy vehicles," *IEEE Access*, vol. 10, pp. 31538–31547, 2022.

[7] J. Wang, Z. Wang, P. Liu, H. Xu, D. Guo, and W. Wei, "Differential drive collaborative steering control of independent-wheel-drive articulated-steering electric vehicles for energy saving," *IEEE Trans. Transpoer. Electrific.*, vol. 10, no. 2, pp. 4142–4158, Jun. 2024.

[8] Y. Yin, S. Rakheja, and P.-E. Boileau, "Multi-performance analyses and design optimisation of hydro-pneumatic suspension system for an articulated frame-steered vehicle," *Vehicle Syst. Dyn.*, vol. 57, no. 1, pp. 108–133, Jan. 2019.

[9] Y. Gao, Y. Shen, Y. Yang, W. Zhang, and L. Güvenç, "Modelling, verification and analysis of articulated steer vehicles and a new way to eliminate jack-knife and snaking behaviour," *Int. J. Heavy Vehicle Syst.*, vol. 26, no. 3, pp. 375–404, 2019.

[10] E. Regolin, A. Alatorre, M. Zambelli, A. Victorino, A. Charara, and A. Ferrara, "A sliding-mode virtual sensor for wheel forces estimation with accuracy enhancement via EKF," *IEEE Trans. Veh. Technol.*, vol. 68, no. 4, pp. 3457–3471, Apr. 2019.

[11] N. Sun, W. Zhang, and J. Yang, "Integrated path tracking controller of underground articulated vehicle based on nonlinear model predictive control," *Appl. Sci.*, vol. 13, no. 9, pp. 5340–5360, Apr. 2023.

[12] M. Yang, Y. Bian, G. Liu, and H. Zhang, "Path tracking control of an articulated road roller with sideslip compensation," *IEEE Access*, vol. 8, pp. 127981–127992, 2020.

[13] N. Daher and M. Ivantysynova, "Yaw stability control of articulated frame off-highway vehicles via displacement controlled steer-by-wire," *Control Eng. Pract.*, vol. 45, pp. 46–53, Dec. 2015.

[14] T. Xu, Y. Shen, Y. Huang, and A. Khajepour, "Study of hydraulic steering process for articulated heavy vehicles based on the principle of the least resistance," *IEEE/ASME Trans. Mechatronics*, vol. 24, no. 4, pp. 1662–1673, Aug. 2019.

[15] T. Xu, Y. Shen, and W. Zhang, "In-situ steering dynamics analysis of skid steering for articulated motor-driven vehicle," *SAE Int. J. Passenger Cars-Mech. Syst.*, vol. 9, no. 2, pp. 903–911, Apr. 2016.

[16] X. Wang, J. Yang, L. Quan, X. Zhang, and J. Wang, "A novel high-efficiency wheel loader power steering system with fault-tolerant capability," *IEEE Trans. Veh. Technol.*, vol. 67, no. 10, pp. 9273–9283, Oct. 2018.

[17] T. Xu, X. Ji, and Y. Shen, "A novel assist-steering method with direct yaw moment for distributed-drive articulated heavy vehicle," *Proc. Inst. Mech. Eng., K, J. Multi-Body Dyn.*, vol. 234, no. 1, pp. 214–224, Mar. 2020.

[18] M. Iida, H. Nakashima, H. Tomiyama, T. Oh, and T. Nakamura, "Small-radius turning performance of an articulated vehicle by direct yaw moment control," *Comput. Electron. Agricult.*, vol. 76, no. 2, pp. 277–283, May 2011.

[19] G. Gao, J. Wang, T. Ma, W. Liu, and T. Lei, "Multistage estimators for the distributed drive articulated steering vehicle," *Math. Problems Eng.*, vol. 2020, pp. 1–16, Oct. 2020.

[20] H. Cherouat and S. Diop, "An observer and an integrated braking/traction and steering control for a cornering vehicle," in *Proc., Amer. Control Conf.*, New York, NY, USA, 2005, pp. 2212–2217.

[21] N. Lashgarian Azad, A. Khajepour, and J. McPhee, "Robust state feedback stabilization of articulated steer vehicles," *Vehicle Syst. Dyn.*, vol. 45, no. 3, pp. 249–275, Mar. 2007.

[22] W.-P. Fang and X.-J. Yang, "Study on driving stability control of electrically driven articulated vehicle," in *Proc. 5th Int. Conf. Electromechanical Control Technol. Transp. (ICECTT)*, Los Alamitos, CA, USA, May 2020, pp. 6–10.

[23] Y. Gao, Y. Shen, T. Xu, W. Zhang, and L. Güvenç, "Oscillatory yaw motion control for hydraulic power steering articulated vehicles considering the influence of varying bulk modulus," *IEEE Trans. Control Syst. Technol.*, vol. 27, no. 3, pp. 1284–1292, May 2019.

[24] T. Xu, X. Ji, Y. Liu, and Y. Liu, "Differential drive based yaw stabilization using MPC for distributed-drive articulated heavy vehicle," *IEEE Access*, vol. 8, pp. 104052–104062, 2020.

[25] Q. Shi and H. Zhang, "An improved control-oriented tire model and its applications on intelligent vehicles," *IEEE Trans. Intell. Vehicles*, vol. 9, no. 1, pp. 1501–1511, Jan. 2024.

[26] Y. Jiang, P. Wu, J. Zeng, X. Wu, Y. Zhang, Z. Yang, R. Gao, and X. Dai, "Researches on the resonance of a new type of suspended monorail vehicle-bridge coupling system based on modal analysis and rigid-flexible coupling dynamics," *Vehicle Syst. Dyn.*, vol. 59, no. 1, pp. 135–154, Jan. 2021.

[27] G. Bai, C. Bao, J. Wu, D. Wu, J. Zhang, and X. He, "A robust guiding torque control method for automatic steering using LMI algorithm," *IEEE Access*, vol. 8, pp. 22162–22169, 2020.

[28] L. Pan, Z. Li, J. Zhang, and Y. Pang, "Frequency-locked loop based on active noise cancellation syncretized two first-order low pass filters," *IEEE Access*, vol. 10, pp. 7277–7288, 2022.

[29] Y. Hao, Z. XiaoYan, C. MingYang, and C. Fei, "Application of energy storage allocation model in the context of mitigating new energy source power fluctuation," *Energy Rep.*, vol. 10, pp. 4791–4799, Nov. 2023.

[30] J. Tian, Q. Wang, J. Ding, Y. Wang, and Z. Ma, "Integrated control with DYC and DSS for 4WID electric vehicles," *IEEE Access*, vol. 7, pp. 124077–124086, 2019.

[31] M. Kuslits and D. Bestle, "Multiobjective performance optimisation of a new differential steering concept," *Vehicle Syst. Dyn.*, vol. 60, no. 1, pp. 73–95, Jan. 2022.

[32] P. Kremer, J. L. Sanchez-Lopez, and H. Voos, "A hybrid modelling approach for aerial manipulators," *J. Intell. Robotic Syst.*, vol. 105, no. 4, pp. 74–95, Aug. 2022.

[33] Y. Gao, D. Cao, and Y. Shen, "Path-following control by dynamic virtual terrain field for articulated steer vehicles," *Vehicle Syst. Dyn.*, vol. 58, no. 10, pp. 1528–1552, Oct. 2020.

[34] S. Latif, T. Lindbäck, H. Lideskog, and M. Karlberg, "Outdoor tests of autonomous navigation system based on two different reference points of PurePursuit algorithm for 10-ton articulated vehicle," *IEEE Access*, vol. 12, pp. 8413–8421, 2024.

[35] S. Zhong, D. Peng, B. Huang, and L. Ma, "Path-tracking ability of the ASV on different adhesion coefficient roads based on slide mode control," *Electronics*, vol. 13, no. 1, p. 105, Dec. 2023.

ZHIYONG JI received the B.S. degree in vehicle engineering from Luoyang Institute of Science and Technology, Luoyang, China, in 2015, and the M.S. degree in vehicle engineering from Taiyuan University of Technology, Taiyuan, China, in 2019, where he is currently pursuing the Ph.D. degree in mechanical engineering. He focuses on vehicle intelligent control and autonomous driving technology.

ZHONGBIN WU received the Ph.D. degree from China Agricultural University, China, in 2020. He is currently a Lecturer with the Department of Vehicle Engineering, Taiyuan University of Technology, China. His research interests include integrated control of vehicle dynamics and vehicle control unit development.

HAOWEN LI received the B.S. degree in vehicle engineering from Xihua University, Chengdu, China, in 2023. He is currently pursuing the master's degree in vehicle engineering with Taiyuan University of Technology, Taiyuan, China. His current research interest includes articulated vehicle path tracking control.

YANSONG ZHAO received the B.S. degree in vehicle engineering from Shandong University of Technology, China, in 2022. He is currently pursuing the master's degree in mechanical engineering with Taiyuan University of Technology, Taiyuan, China. He focuses on chassis control by wire for articulated vehicles.

TIE WANG received the B.S. and M.S. degrees in mechanical engineering from Taiyuan University of Technology (TYUT), Taiyuan, China, in 1979 and 1989, respectively, and the Ph.D. degree in mechanical design and automation from Beijing Institute of Technology (BIT), Beijing, China, in 2005. He is currently a Professor and the Director of TYUT. His research interests include mechanical transmission and dynamics, modern automotive design and vehicle dynamics, clean fuel engines, hybrid power systems, and autonomous driving technology.